NORTHWESTERN
UNIVERSITY

Center for Sustainable Engineering of Geological and Infrastructure Materials (SEGIM)

Department of Civil and Environmental Engineering

McCormick School of Engineering and Applied Science

Evanston, Illinois 60208, USA

AGE-DEPENDENT SIZE EFFECT AND FRACTURE CHARACTERISTICS OF ULTRA HIGH PERFORMANCE CONCRETE

Lin Wan, Roman Wendner, Gianluca Cusatis

SEGIM INTERNAL REPORT No. 16-08/465A

August 2016

Age-dependent Size Effect and Fracture Characteristics of Ultra High Performance Concrete

By

Lin Wan [1], Roman Wendner* [2], Gianluca Cusatis [3]

A Paper To Be Submitted

August 31, 2016

Corresponding Author

Roman Wendner

Director - Christian Doppler Laboratory LiCRoFast

Department of Civil Engineering and Natural Hazards

University of Natural Resources and Life Sciences (BOKU)

Peter Jordan Strasse 82, A-1190

Vienna, Austria

Tel: +43 1 47654 5252

Fax: +43 1 47654 5299

Email: roman.wendner@boku.ac.at

Website: http://www.baunat.boku.ac.at/cd-labor

[1]Ph.D., Researcher, Department of Civil and Environmental Engineering, Northwestern University, 2145 Sheridan Rd. Evanston IL, 60208 USA. E-mail: lin.wan@u.northwestern.edu

[2]Corresponding Author: Director Christian Doppler Laboratory LiCRoFast, Department of Civil Engineering and Natural Hazards, University of Natural Resources and Life Sciences (BOKU) Vienna. E-mail: roman.wendner@boku.ac.at

[3]Associate Professor, Department of Civil and Environmental Engineering, Northwestern University, 2145 Sheridan Rd. Evanston IL, 60208 USA. E-mail: g-cusatis@northwestern.edu, Phone: (847)-491-4027

Abstract:

This paper presents an investigation of the age dependent size effect and fracture characteristics of an ultra high performance concrete (UHPC). Experiments and simulations are conducted according to the age dependent and discrete element based theoretical framework, HTC-LDPM, developed in the authors' previous work [1]. The aging framework is formulated by coupling a hygro-thermo-chemical (HTC) theory with the Lattice Discrete Particle Model (LDPM). The HTC component allows taking into account variable curing conditions and predicting the maturity of concrete, while the mechanical component, LDPM, permits the simulation of the failure behavior of concrete at the length scale of major heterogeneities. By well calibrated and validated HTC model and LDPM bridged by aging functions, size effect simulations and predictions of various early ages and sizes are carried out, in furtherance of an experimental campaign, for the UHPC. The ultimate three-point-bending flexural strengths from experiments and simulations are analyzed by cohesive size effect curve (CSEC) method and classical size effect law (SEL). The CSEC method fits slightly better than SEL, while both with correlation R^2 values higher than 0.99. Based on experiments, simulations, size effect analysis, and the formulated aging functions, it is concluded that the fracture energy can have a non-monotonic relation in terms of concrete aging. Furthermore, it is found that the magnitude of size effect increases with concrete aging. In other words, mature concrete exhibit higher size effect than young concrete. With great accuracy and prediction significance in simulating mechanical behavior, the HTC-LDPM framework can be applied to a broad range of cement based concrete materials for aging and size effect studies.

1 Introduction

Ultra high performance concretes (UHPCs) are cementitious composites characterized by high compressive strength, low water-binder ratio, optimized gradation curve, inclusion of thermal activation, fiber reinforcement and superplasticizers. UHPC became commercially available in the beginning of the 21st century and has been utilized in the construction industry, especially for bridge applications and tall buildings, around the world across North America, Europe, and Asia. While more and more UHPCs are developed and utilized in the construction industry, what is lacking in the available literature is a model for the evolution of fracture characteristics and size effect of UHPCs at early age. This is crucial in terms of structural design, project planning, and building

optimization. Based upon the formulated early age mode in the authors' previous work [1], this paper presents a comprehensive size effect study and analyzes the age dependent fracture characteristics for a UHPC.

It is well known that the strength of cementitious concrete increases rapidly at early age. However, the chemical and physical mechanisms behind this phenomenon are complex and consist of multiple coupled components. The cross-effects between hydration reaction, temperature and humidity evolution, and member deformation involve complex chemo-physical mechanisms that operate over a broad range of length and time scales. Notably, evolution laws for maturing concrete based on Arrhenius-type time acceleration concepts are widely supported by a good agreement with experimental data [42, 43, 36].

Ulm and Coussy [36] studied the thermo-chemo-mechanical coupling of concrete at early age with a formulation based upon thermodynamics of open porous media composed of a skeleton and several fluid phases saturating the porous space. It accounts explicitly for the hydration of cement by considering the thermodynamic imbalance between the chemical constituents in the constitutive model at the macrolevel, however neglecting the effects from stress and temperature evolutions. Afterwards they extended the thermo-chemo-mechanical cross effects characterizing the autogeneous shrinkage, hydration heat and strength growth, within the framework of chemoplasticity [32]. Cervera et. al. [28] applied the reactive porous media theory and introduced a novel aging model which accounts for the effect of curing temperature evolution featuring the aging degree as an internal variable. They suggested that the evolution of the compressive and tensile strengths and elastic moduli can be predicted in terms of the aging degree [26, 27]. The model considers the short-term mechanical behavior based on the continuum damage mechanics theory and the long-term mechanical behavior based upon the microprestress-solidification theory [29]. Bernard, Ulm and Lemarchand [25] developed a multi scale micromechanics-hydration model to predict the aging elasticity of cement-based materials starting at the nano level of the C-S-H matrix. Lackner and Mang [23] proposed a 3-D material model for the simulation of early-age cracking of concrete based on the Rankine criterion formulated in the framework of multi surface chemoplasticity. Gawin, Pesavento, and Schrefler [20, 21] proposed a solidification-type early-age model and extended it to account for coupled hygro-thermo-chemo-mechanical phenomena, which was already applied to practical problems [8, 7].

Di Luzio and Cusatis [15, 16] formulated, calibrated, and validated a hygro-thermo-chemical (HTC) model suitable for the analysis of moisture transport and heat transfer for standard as well as high performance concrete.

In this study, classical macroscopic mass and energy conservation laws were formulated in terms of humidity and temperature as primary variables and by taking into account explicitly various chemical reactions including cement hydration, silica fume reaction, and silicate polymerization [15]. Furthermore, Di Luzio and Cusatis [9], amalgamated the microplane model and the microprestress-solidification theory. This unified model takes into account all the most significant aspects of concrete behavior, such as creep, shrinkage, thermal deformation, and cracking starting from the initial stages of curing up to several years of age.

While continuum mechanics and finite element solvers are broadly utilized for mechanical analysis of concrete structures at the macroscopic levels, the Lattice Discrete Particle Model (LDPM) [10, 11] provides additional insights into failure behavior of concrete at smaller length scales. LDPM simulates concrete at the length scale of coarse aggregate pieces (mesoscale) and is formulated within the framework of discrete models, which enable capturing the salient aspects of material heterogeneity while keeping the computational cost manageable [10].

The HTC model and LDPM are selected as basis for the early age mechanical model formulated in the authors' previous work [1]. By coupling the hygro-thermo-chemical (HTC) model and the Lattice Discrete Particle Model (LDPM) bridged by aging functions, the proposed computational framework can accurately simulate the development of the internal structure of C-S-H reactions and corresponding effects on mechanical properties. The developed aging functions for the investigated UHPC connecting the HTC model and LDPM have a quite simple form but capture fully the evolution of material properties as functions of aging degree. The details of the computational framework can be found in Wan et. al [1] and are summarized in Appendix B.

In furtherance of aging, size effect of quasi brittle infrastructure materials, e.g. concrete, is crucial in structural design and construction. In many situations, e.g. shear design of beams, laboratory scale mechanical tests can not represent the structural level performance without taking into consideration the size effect. Furthermore, the fracture properties evolution of concrete during aging play a significant role in design and construction planning. In the literature, a limited number of studies of the age-dependent fracture characteristics are available [31, 24, 22], however a computational framework capable of comprehensively capturing and predicting the age dependent fracture characteristics is still missing. Moreover, although size effect has long been widely known in the civil engineering community, its age dependence has not been studied in the available literature. Thus, the developed HTC-LDPM framework is applied to assess its ability in describing the age dependence of size effect and fracture characteristics.

Size effect studies are carried out by experiments, simulations, predictions and fracture analysis. Fully cured UHPC beams with scaled geometries were utilized in three-point-bending tests. Data of beams of one size but on various ages are available from previous studies [1]. Within the computational framework of HTC-LDPM, validations and predictions are carried out for various early ages and scaled specimen sizes. The nominal flexural strengths obtained from experiments and predictive simulations are then analyzed by various methods including the SEL (size effect law) and CSEC (cohesive size effect curves) method. The tensile strength and tensile characteristic length can be directly obtained through data fitting by SEL and CSEC. Afterwards the initial and total fracture energy is computed and further analyzed in terms of aging. The stress field orthogonal to the crack and associated dissipated energy for various sizes and ages are as well computed and presented. Lastly, the magnitude of size effect is evaluated in terms of concrete aging.

2 Literature Review on Size Effect

The mechanical size effect of quasi-brittle materials, e.g. concrete, rock, ceramics, etc., has been broadly described in the literature as the dependence of the structural strength on the structural size. More specifically, the structural strength, a normalized measure of the load-carrying capacity of the structure, decreases as the structural size increases. In the case of beam specimens under three-point-bending (TPB) tests, the structural flexural nominal stress σ_N can be defined as:

$$\sigma_N = \frac{3PS}{2BD^2} \tag{1}$$

where P = load, S = specimen span, B = specimen thickness, and D = specimen depth [30].

Based on the cohesive crack model, with a linear softening law, the size effect for mode I fracture can be described by the following equation [33, 18]:

$$\left(\frac{f'_t}{\sigma_{Nu}}\right)^2 = \Phi\left(\frac{D}{\ell_{ch}}\right) \tag{2}$$

where f'_t = tensile strength, σ_{Nu} = nominal strength associated with the peak load P_u, D = size of structural member, and ℓ_{ch} is Hillerborg's characteristic length: $\ell_{ch} = EG_F/f_t'^2$, E = Young's modulus, and G_F = total fracture energy (energy required to create a unit area of stress-free crack). The approximation of Φ can be

obtained by carrying out numerical simulations of cohesive crack propagation in geometrically similar structures. Following Cusatis and Schauffert [13], size effect relationships represented symbolically by Eq. 2, and all other similar relationships involving normalized ultimate nominal stress as a function of normalized structural size, will be termed *cohesive size effect curves* and abbreviated "CSEC".

On the other hand, with no reference to the cohesive crack model [13], the size effect law (SEL), first formulated by Bažant in 1984 [41], can be derived on the basis of equivalent linear elastic fracture mechanics (LEFM). The LEFM crack initiation condition is written with reference to an "effective crack length" as $G(\alpha_0 + c_F/D) = \sigma_{Nu}^2 D g(\alpha_0 + c_F/D)/E = G_F$, where $G(\alpha)$ = energy release rate, $\alpha_0 = a_0/D$ is the initial dimensionless notch depth, a_0 = initial notch depth, $g(\alpha)$ = dimensionless energy release rate, and c_F = effective fracture process zone length, assumed to be a material property [30, 13]. By approximating $g(\alpha_0 + c_F/D)$ with its Taylor series expansion at α_0 and retaining only up to the linear term of the expansion, the classical form of Bažant's SEL can be obtained:

$$\sigma_{Nu} = \sqrt{\frac{EG_F}{g_0' c_F + g_0 D}} \tag{3}$$

where g_0 is the dimensionless energy release rate and g_0' is its derivative for $\alpha = \alpha_0$. By introducing Hillerborg's characteristic length, ℓ_{ch}, Bažant's SEL, can be recast into the following form:

$$\left(\frac{f_t'}{\sigma_{Nu}}\right)^2 = g_0 \frac{D}{\ell_{ch}} + g_0' \frac{c_F}{\ell_{ch}} \tag{4}$$

As already proven by previous analytical and numerical studies [13, 40, 38], the SEL is equivalent to the asymptotic behavior of the CSEC, namely the CSEC tends asymptotically to a straight line for large sizes that corresponds to the SEL. For a nonlinear softening law and for realistic structural sizes, it can be shown that Eq. 2∼4 still apply, if one considers the initial fracture energy G_f characterizing the initial part of the softening law (see Fig. 9d) and the associated characteristic length $\ell_1 = EG_f/f_t'^2$.

To facilitate the identification of G_f and ℓ_1 through the CSEC, an approximated analytical CSEC formula for TPB geometries was developed to match both the small-size (plastic limit) and large-size (asymptotic) behaviors [13]. This approximately has the following form:

$$\frac{f_t'^2}{g_0' \sigma_{Nu}^2} = \frac{g_0 D}{g_0' \ell_1} + \left(1 + 11\sqrt{\frac{g_0 D}{g_0' \ell_1}}\right)\left(\beta_0 + 25\sqrt{\frac{g_0 D}{g_0' \ell_1}}\right)^{-1} \tag{5}$$

where $\beta_0 = 9(1-\alpha_0)^4 g_0'$. The associated SEL [13] is:

$$\frac{f_t'^2}{g_0' \sigma_{Nu}^2} = \frac{g_0 D}{g_0' \ell_1} + 0.44 \tag{6}$$

3 UHPC Size Effect Study

3.1 Experiments

Mix-design and curing protocol for the UHPC material utilized in this size effect study was described in Wan. et. al. [1] and is summarized in Appendix A. Three sets of beams were cast with a geometrical scaling factor of $\sqrt{5}$ for depth & span and constant thickness of 25.4 mm (1 in). Their nominal dimensions are as follows: size M, 25.4×25.4×127 mm (1×1×5 in); size L, 56.8×25.4×254 mm ($\sqrt{5}$×1×10 in); size XL, 127×25.4×558.8 mm (5×1×22 in). The depth to span ratio was kept as 1:4. On 120 days of average age, the specimens were machined to have 50% notch depth, and were tested in a TPB configuration in crack-mouth-opening-displacement (CMOD) control as shown in Fig. 1a. The actual dimensions measured on the day of testing are utilized for post-test calculations and are listed in Table 1. The testing results are shown in Fig. 1b, in which the nominal flexural stress is computed based on Eq. 1, the nominal strain is calculated by $\epsilon_N = CMOD/D$, and the total fracture energy G_F, according to the work of fracture, is computed as the area under the force-displacement curve divided by the ligament area. As one can see, the nominal strength reduces significantly with size and the total fracture energy is approximately constant with an average value of G_F^{exp}=63.3 J/m^2.

Table 1: Actual specimen dimensions for size effect tests

Size	Length L [mm]	Thickness B [mm]	Depth D [mm]	Test Span S [mm]	No. of Specimens
M	128.0±0.2%	26.3±1.9%	26.2±1.1%	101.6	8
L	254.1±0.4%	26.5±4.6%	58.0±0.7%	227.2	4
XL	558.2±0.0%	26.5±4.3%	127.3±0.9%	508	3

3.2 LDPM Simulations

The size-effect experiments were simulated through an age-dependent mesoscale computational framework [1, 2], derived by coupling the hygro-thermo-chemical (HTC) model [15, 16, 9] and the Lattice Discrete Particle Model (LDPM) [10, 11]. The details of the computational framework can be found in Wan et. al [1] and are summarized in Appendix B. The LDPM parameters computed through the aging functions for the nominally 120

(a)

(b)

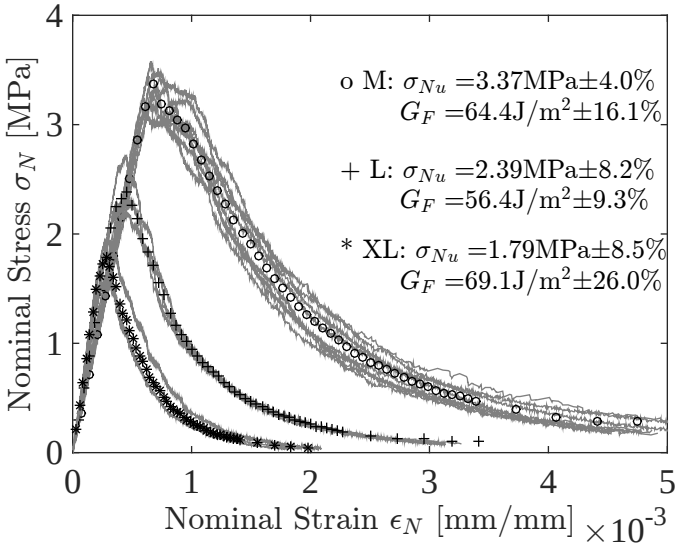

Figure 1: UHPC size effect experimental (a) test setup and (b) testing results: nominal stress-strain curves of three point bending tests

days old UHPC specimens are listed in Table 2 where the LDPM parameters governing the tensile fracturing behavior are underlined. It must be observed here that the parameters reported in Table 2 where identified on the basis of the TPB tests of medium size along with data on unconfined compression behavior [1, 6, 4]. Consequently, the simulations of large (L) and extra-large (XL) specimens must be regarded as pure predictions. Simulation setup as well as crack patterns are as shown in Fig. 2. In order to save computational cost, the middle section of the specimen of length equal to the specimen depth is simulated through the mesoscale model whereas the rest of the specimen is simulated with elastic finite elements. Continuity at the interfaces was enforced by means of a master-slave algorithm.

The LDPM simulation results as well as crack patterns for each size can be found in Fig. 3. At least three specimens with different particle placement were utilized for each size to show the scatter due to random particle placement. The simulations have slightly higher stress values compared to the experimental data. This is most likely due to shrinkage cracking of the specimens tested experimentally, which is not considered in the current numerical analysis. The fracture energy from simulations are calculated as the area under the force-displacement curve divided by the nominal ligament area. Note the G_F^{sim} values in Fig. 3 are computed after truncating the simulated force-displacement curves with equivalent crack mouth opening as in the experiments. G_F^{sim} has an average value of 68.3 J/m^2, which is about 7.9% higher than that of the experiments, G_F^{exp}=63.3 J/m^2. When the full force-displacement curve is considered, G_F^{sim} has a value of about 100.6 J/m^2. Overall, the simulations

can represent the UHPC behavior under TPB test with very high accuracy and capture the experimentally observed size effect for fully cured specimens. The crack patterns from simulations also coincide with those of the TPB experiments. In an earlier study the capability of the framework to well reproduce the age dependent response was shown [1]. Thus, it can be assumed that the model can also predict well the age dependence of size effect.

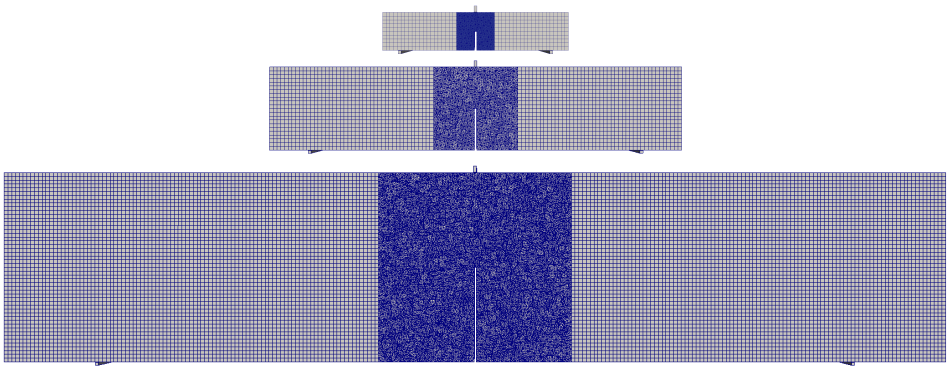

Figure 2: UHPC size effect LDPM simulation setup (top to bottom: M, L, XL)

Table 2: Size Effect - LDPM Parameters

Days	120 (HR+WB)
Ave. Aging Degee	0.9546
±Standard Deviation [%]	±0.010
Normal Modulus E_0 [MPa]	71595
Densification Ratio E_d/E_0 [-]	2.5
Alpha [-]	0.25
Tensile Strength σ_t [-] [MPa]	11.9
Compressive Yielding Stress [MPa]	449
Shear Strength Ratio [-]	5.5
Tensile Characteristic Length ℓ_t [mm]	21
Fracture Energy G_t [J/m^2]*	21.13
Softening Exponent [-]	0.28
Initial Hardening Modulus Ratio [-]	0.36
Transitional Strain Ratio [-]	4
Inital Friction [-]	0.0335
Asymptotic Friction [-]	0
Transitional Stress [MPa]	269
Volumetric Deviatoric Coupling [-]	0
Deviatoric Strain Threshold Ratio [-]	1
Deviatoric Damage Parameter [-]	5

* Calculated as $G_t = \ell_t \sigma_t^2 / 2E_0$

3.3 Size Effect Analysis

In this section CSEC & SEL (Eq. 5&6) are fitted to the experimental and numerical nominal strengths in order to identify macroscopic fracture properties (f_t', ℓ_1, G_f) and assess the reliability of such identification procedure. For a single-edge cracked beam subjected to three-point bending, the expression for fracture analysis depends mildly on the shear force magnitude near the central cross-section, i.e., on the span-to-depth ratio [30]. For the case S/D=4 as in this study, the dimensionless energy release rate can be calculated, according to Pastor et al. [37, 14], as $g(\alpha) = k(\alpha)^2$, $k(\alpha) = \sqrt{\alpha}p(\alpha)/((1 + 2 * \alpha)(1 - \alpha)^{1.5})$, and $p(\alpha) = 1.900 - \alpha[-0.089 + 0.603(1 - \alpha) - 0.441(1 - \alpha)^2 + 1.223(1 - \alpha)^3]$.

For 50% notched beams, $\alpha_0 = 0.5$, and one has $g_0 = 3.1415$, $g_0' = 19.858$. The fitted CSEC & SEL curves for experimental and simulated ultimate strengths are presented in Fig. 4a&b respectively. The axes $X = g_0 D/g_0' \ell_1$ and $Y = f_t'^2/g_0' \sigma_{Nu}^2$ are taken as in Eq. 5&6. The two parameters: tensile strength, f_t', and tensile characteristic length, ℓ_1, are obtained through the CSEC & SEL data fitting. The initial fracture energy is calculated as $G_f = \ell_1 f_t'^2/E$ using the correspondingly fitted values (f_t', ℓ_1) of CSEC & SEL. Note, in the figure the SEL lines are normalized based on CSEC fits for comparison reasons. Both CSEC and SEL fit the size effect data very well with correlation coefficients higher than 0.99, whereas CSEC fits slightly better than SEL. The CSEC fitted tensile strength is on average 20% lower than the SEL fitted value; The CSEC fitted tensile characteristic length is about 40% higher than that of SEL; The calculated initial fracture energy for CSEC is roughly 4.8% higher than that for SEL. When compared to the LDPM parameters σ_t & f_t' (see Table 2), the CSEC fitted f_t' & ℓ_1 (see Fig. 4b) are 10.9% lower and 17.6% lower respectively, and the SEL fitted values are 16.0% higher and 54.3% lower respectively. Overall, the CSEC provides closer values than SEL when compared to the LDPM parameters; The SEL tends to overestimate the tensile strength and largely underestimate the tensile characteristic length; The asymptotic behavior of CSEC and SEL tend to coincide with each other. In conclusion, both CSEC and SEL can provide highly accurate fits, however the CSEC is more reliable than SEL in terms of providing fracture related parameter values from data fitting, especially for smaller sizes that start deviating from the asymptotic shape.

3.4 Sensitivity Study of CSEC

As shown in Fig. 3, the simulations are fairly close to the experimental data, well representing the actual crack propagation. The average nominal strength from simulations for size M, L and XL are 3.1%, 9.5% and 8.8% higher than those of the experiments respectively. This section focuses on the discussion of the differences of the CSEC analysis for the experimental and simulated results.

As shown in Fig. 4, the simulated ultimate strengths are fitted by CSEC with R^2 value of 99.99%; Similarly, the experimental data points are matched with $R^2 = 99.48\%$, indicating the excellent capability of CSEC in describing the size effect of concrete. However, the CSEC fitted parameters (f_t', ℓ_1, G_f) for the experimental results differ moderately from those for the simulated set of data. CSEC fitted f_t' for experiment is 15% higher than that for simulation. CSEC fitted ℓ_1 for experiment is 42% lower than that for simulation. The correspondingly calculated G_f for experiment is about 24% than that for simulation.

To study the sensitivity of the CSEC method, 10,000 possible realizations for the ultimate flexural tensile strength, σ_{Nu}, were created. The Monte Carlo method with normal distribution was utilized for sampling both experimental and simulated data sets of σ_{Nu}, while keeping their actual average and standard deviation values. The actual average dimension, D, the depth of the specimens of each size was utilized since its scatter is negligible with standard deviation lower than roughly 1% from experiments. The nominal dimensions were utilized for simulations. Afterwards the CSEC analysis was conducted for each generated sample set, yielding corresponding realizations of tensile strength and tensile characteristic length. The resulting histograms can be found in Fig. 5, along with the correspondingly calculated initial fracture energy, $G_f = \ell_1 f_t'^2/E$.

When comparing results for experiment samples and simulation samples, the following points can be drawn. The average tensile strength obtained for the simulation samples is 50% lower than that for the experiment samples. The average tensile characteristic length of the simulation samples is 15% higher than that of the experiment samples. The average fracture energy for the simulation samples is about 20% higher than that for the experiment samples. As shown in Fig. 5, both f_t' and ℓ_1 of the experiment samples have high standard deviation, which indicates that CSEC is very sensitive to noise in data, with the same level of mean value and scatter. Provided that the LDPM parameters are well calibrated and validated based on a comprehensive experimental campaign [1], the LDPM mesoscale tensile strength, $\sigma_t = 11.9$ MPa, and the tensile characteristic length, $\ell_t = 21$ mm, (see Table 2) can be utilized as reference to evaluate the sensitivity study results. The

tensile strength, $f_t' = 11.4$ MPa, and tensile characteristic length, $\ell_1 = 21.5$ mm, for simulation samples are almost identical with the LDPM parameters. While for experiment samples, $\ell_1 = 18.6$ mm, is 11% lower than σ_t, and $f_t' = 22.2$ MPa, almost doubles f_t'. The high sensitivity of obtaining f_t' by experiment samples can be overcome by excluding the outliers. When putting an upper bound of 40 for fitting tensile strength of the experimental sample, in other words, excluding outliers higher than 40, the average f_t' then drops from 22.2 MPa to 16.9 MPa, with negligible change in fitted average ℓ_1 and G_f. In conclusion, the values of tensile strength and tensile characteristic length from CSEC analysis agree with those adopted in LDPM; In terms of sensitivity, obtaining ℓ_1 and G_f by CSEC is fairly stable against noise in the data; On the other hand, getting f_t' through CSEC can be very sensitive to noise in the data, whereas, exerting upper and lower bounds of the expected range of f_t' can improve its accuracy.

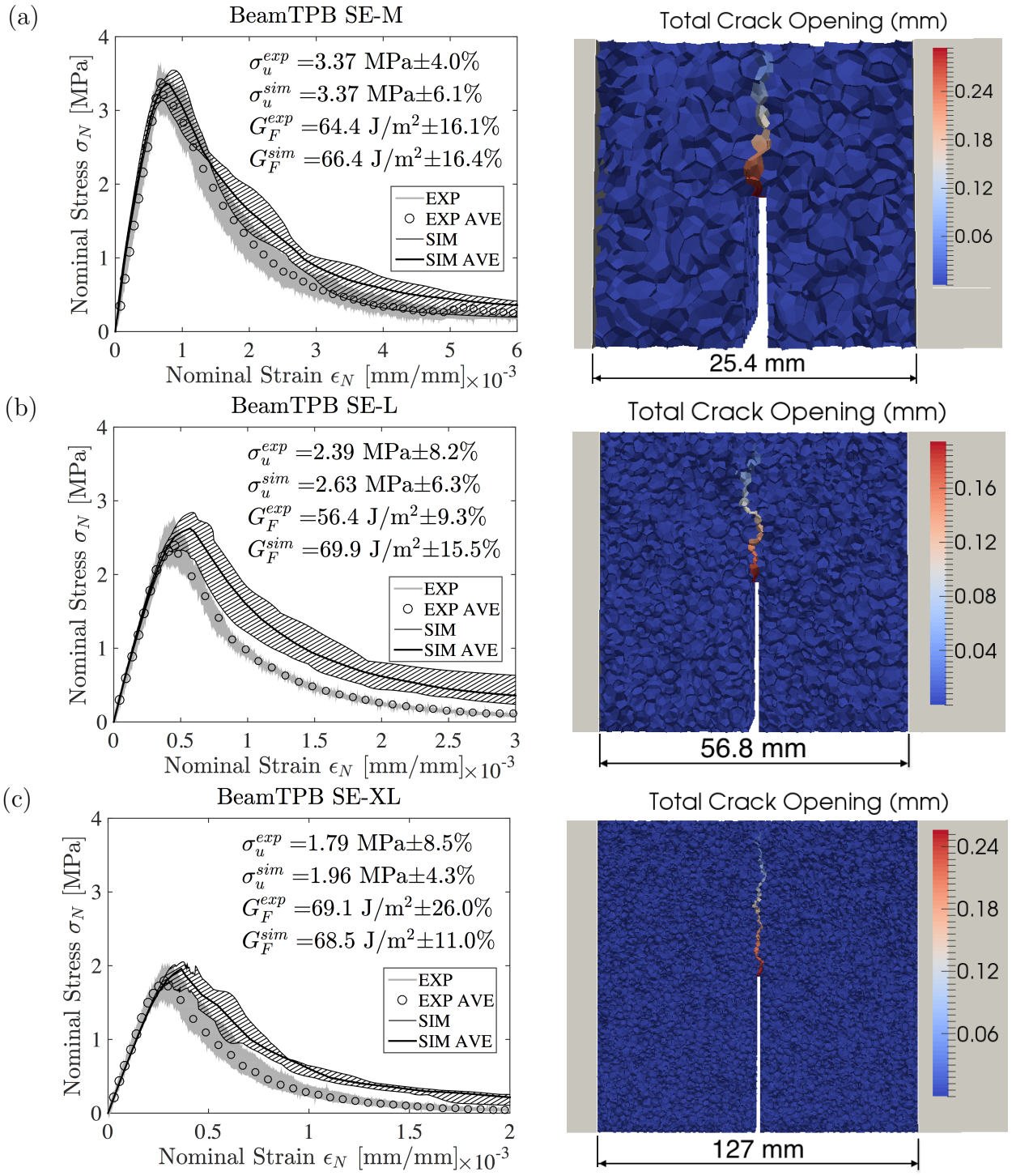

Figure 3: UHPC size effect experiments vs. LDPM simulations and simulated crack propagation for (a) size M (b) size L (c) size XL

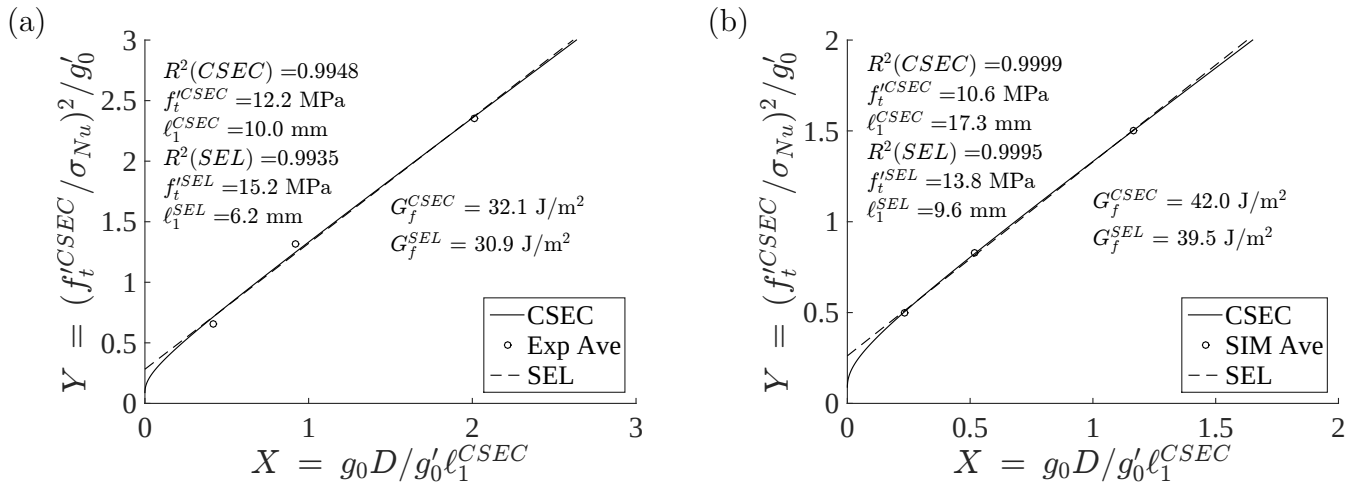

Figure 4: UHPC CSEC and SEL data fitting for (a) experimental and (b) simulated ultimate strengths of size M, L, and XL

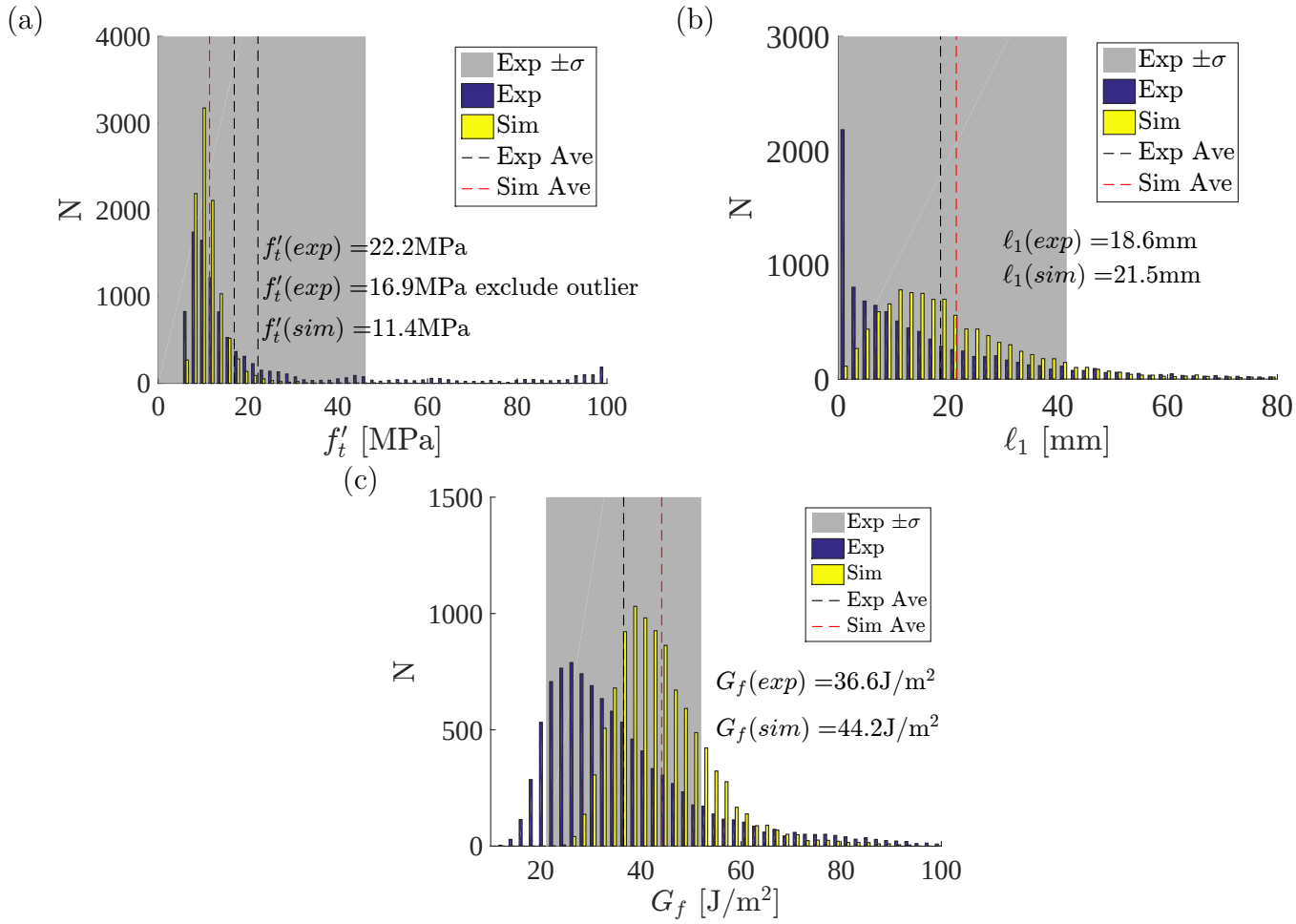

Figure 5: Sensitivity study of CSEC in respect to experimental and simulated peak strength: fitted (1) tensile strength (2) tensile characteristic length (3) initial fracture energy from 10,000 samples

4 HTC-LDPM Simulations and Predictions

Predictive size effect simulations for the UHPC (size M, L, XL, XXL) are carried out for the same early ages as investigated by Wan et al. [1]: HR curing 3, 7, 14, 28 days, and HR+WB curing 14/28 days. Size M, L, XL have the same nominal dimensions as described in the previous sections. The largest size XXL is geometrically upscaled from size L by $\sqrt{5}$ on span and height while keeping the thickness constant. It has the nominal dimensions of 284×25.4×1420 mm ($5\sqrt{5}\times1\times25\sqrt{5}$ in) with span of 1136 mm ($20\sqrt{5}$ in). The simulated stress-strain curves for all sizes and ages are shown in Fig. 6, along with the fitted CSEC & SEL curves for the corresponding early ages. At least five specimens with different discrete particle placement were utilized for each size and age to ensure representative simulation. Size M has a relatively large scatter in the late post-peak phase. Size L shows a relatively large scatter in the ultimate peak stress. In spite of the scatter, the predicted size effect simulations by the HTC-LDPM computational framework show a perfectly decreasing relation of strength in terms of size and increasing trend of strength versus aging. The strength-size relationship for each age can be described very well by both the size effect models CSEC & SEL.

The same procedures as discussed in the previous section of CSEC and SEL analysis (Eq. 5 & 6) are followed. The shape factor, α, initial energy release rate, g_0, and its first order derivative, g_0', remain the same. Tensile strength, f_t', and characteristic length, ℓ_1, are obtained from data fitting, which are then utilized to compute the initial fracture energy, G_f, for each age. Young's modulus for the early ages, indirectly determined by TPB simulations by matching experimental data [1], were utilized to calculate G_f and are listed in Table 3. Hence, the average correlation coefficient R^2 of CSEC for the predicted ultimate strength on different ages is higher than 0.999. In other words, the CSEC analyses highly agree with the HTC-LDPM early age model. The SEL fits have a slightly lower, however also quite high, R^2 value of 0.995, solely lacking the representation of plastic limit end for small sizes.

In order to assess the mesoscale stress level and energy dissipation for the beams of different ages and sizes, the relevant data is extracted from the LDPM simulations. Stress along the ligament, obtained as homogenized stress tensor of each tetrahedron for each simulated age and size by LDPM, is plotted in Fig. 7. The subfigures from left to right are of increasing sizes and from top to bottom are for increasing aging degree. The X axis is the stress level; The Y axis is the normalized ligament height, with value 0 being the initial notch tip and value 1 meaning the top of the specimen. Investigated time-points during each simulated test are at 50% of

peak in the linear section, at peak, 50% post peak and at 20% remaining strength in the post peak. The simulated specimens have the same minimum and maximum aggregate sizes of 2-4 mm. As a result, the larger the specimen size, the smoother the stress profile and the clearer the trend to be observed. By comparing the stress profiles of different ages and sizes, the following observations can be made: the maximum stress level for each age remain the same for different sizes; The maximum stress tensor readings for all sizes increase in terms of aging and are equal to the mesoscale tensile strength of LDPM for the corresponding ages; As the crack propagates, the corresponding section under tension shifts upwards and the top section under compression decreases in terms of height but with increasing compressive stress; The hinge, where zero-stress-point lies at peak strength of each test, is located at about half of the ligament height for all sizes and ages.

Similarly, the accumulated dissipated energy during fracture along the ligament of the investigated sizes and ages are shown in Fig. 8. Corresponding to the stress profiles in Fig. 7, the dissipated energies are plotted at 50% before peak, at peak, 50% post peak and at 20% remaining strength. For each size, the dissipated energy increases in terms of aging degree until humidity curing 28 days and drops for hot water bath curing 28 days. This agrees with the age dependent fracture energy obtained from experiments, calibrated and validated HTC-LDPM simulations, as well as CSEC and SEL analysis, which all conclude that the fracture energy can reach a peak in terms of aging degree. In general, the larger the size, the higher the total dissipated energy is accumulated, which can be estimated as the area under the curves in Fig. 8. However, the maximum dissipated energy level is roughly the same for different sizes if a fracture process zone fully develops. For size XL and XXL, the dissipated energy after peak reaches the maximum value for about 50% of the ligament, indicating that a fracture process zone fully develops. For size L, the maximum dissipated energy level, located at at the notch tip, is roughly the same as of size XL & XXL. This means that, for size L, a fracture process zone develops only close to the notch tip due to its size limit. While for size M, the dissipated energy is lower than the maximum level as of size L, XL & XXL, indicating that a fracture process zone is not fully developed due to its size limit.

Table 3: UHPC Young's Modulus Evolution on Early Age

Age	HR 3d	HR 7d	HR 14d	HR 28d	WB 14/28	WB 120d
E [MPa]	27089	34267	37669	39323	46302	46326

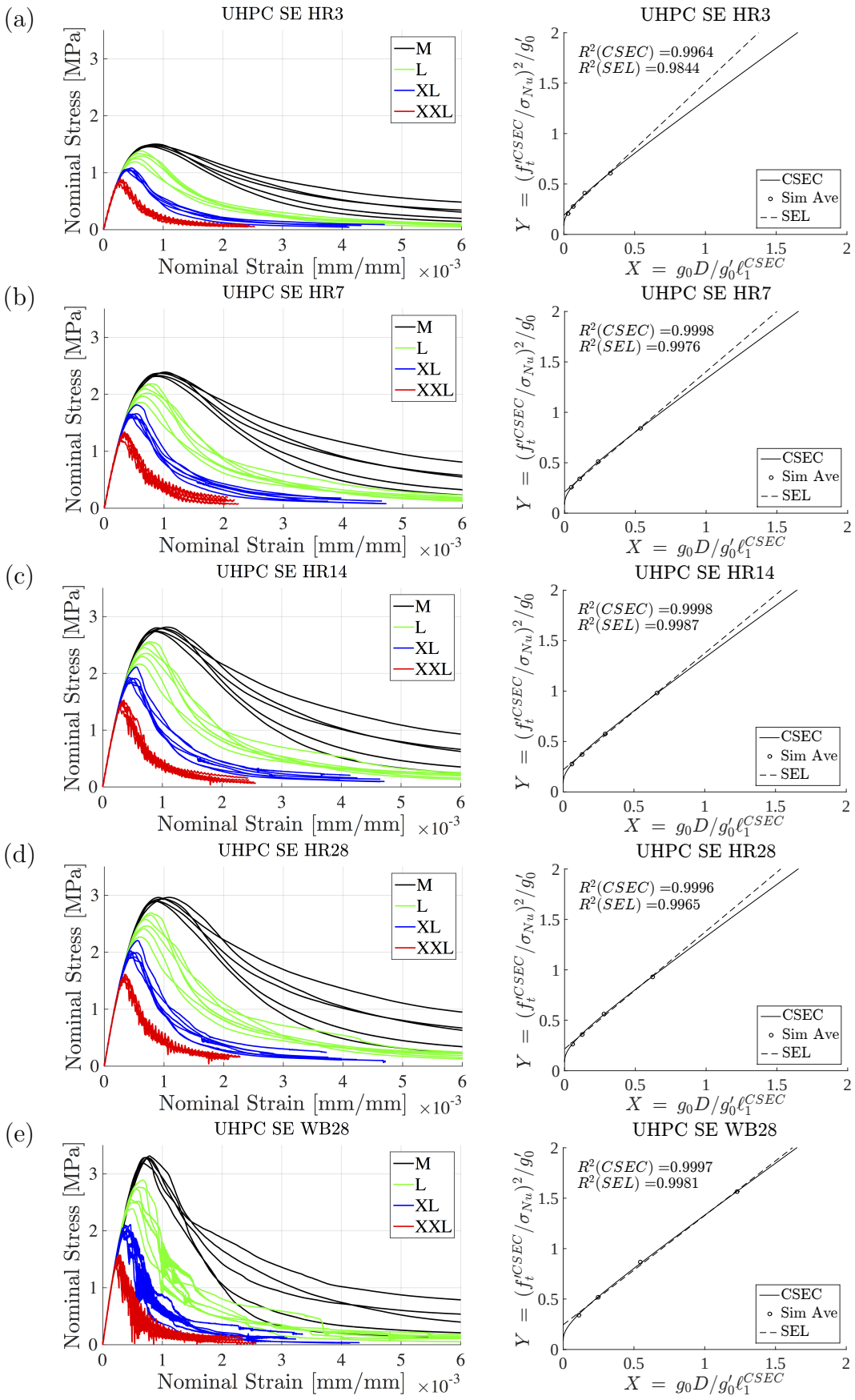

Figure 6: A-LDPM size effect predictions and CSEC & SEL analysis for (a) humidity room (HR) curing 3 days (b) HR 7 days (c) HR 14 days (d) HR 28 days and (e) hot water bath (WB) curing 28 days. SEL curve is normalized based on CSEC fitting

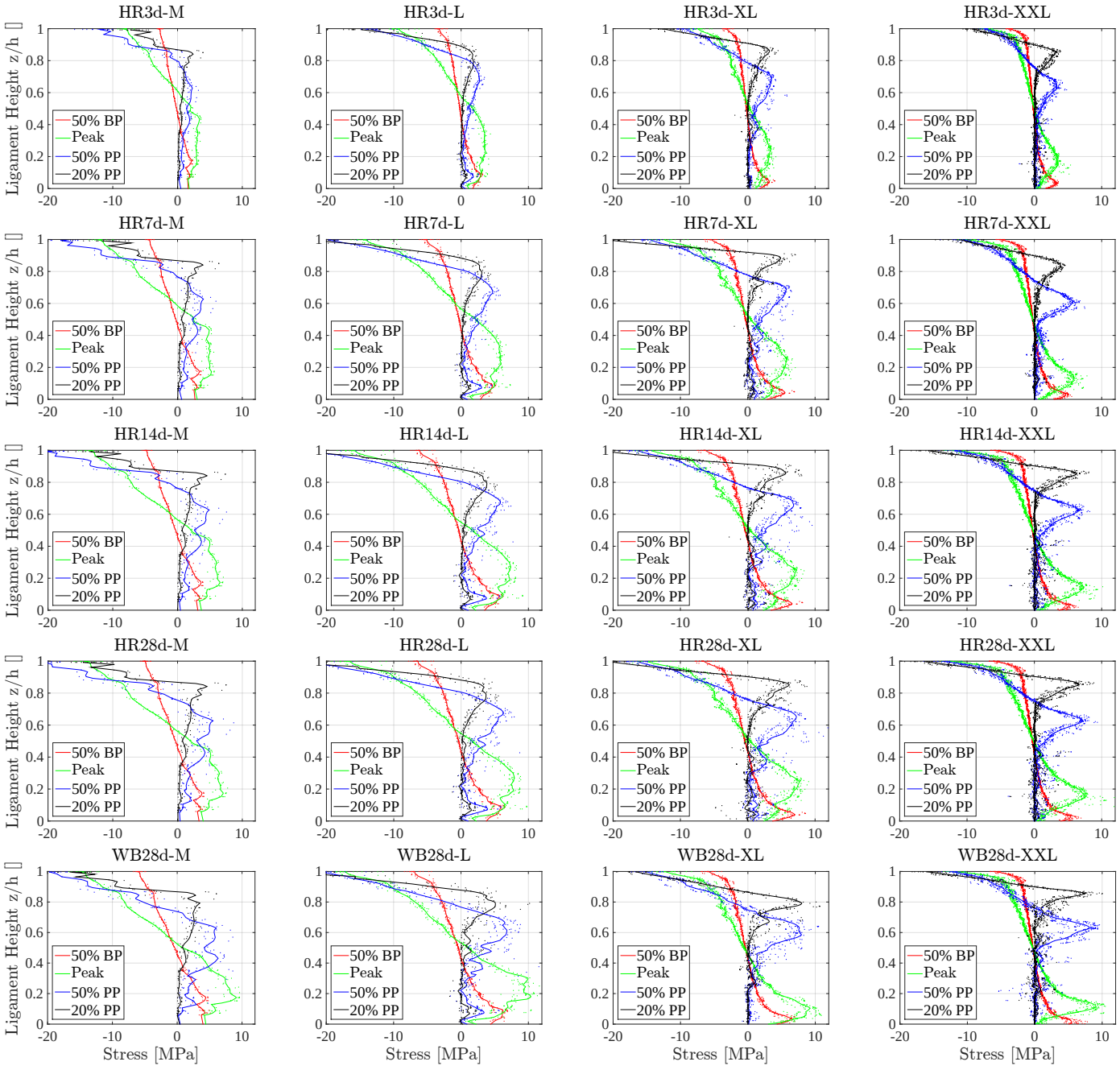

Figure 7: Stress profiles along ligament from A-LDPM simulations for size effect study; from left to right: size M, L, XL, XXL; top to bottom: age HR3d, HR7d, HR14d, HR28d, WB28d

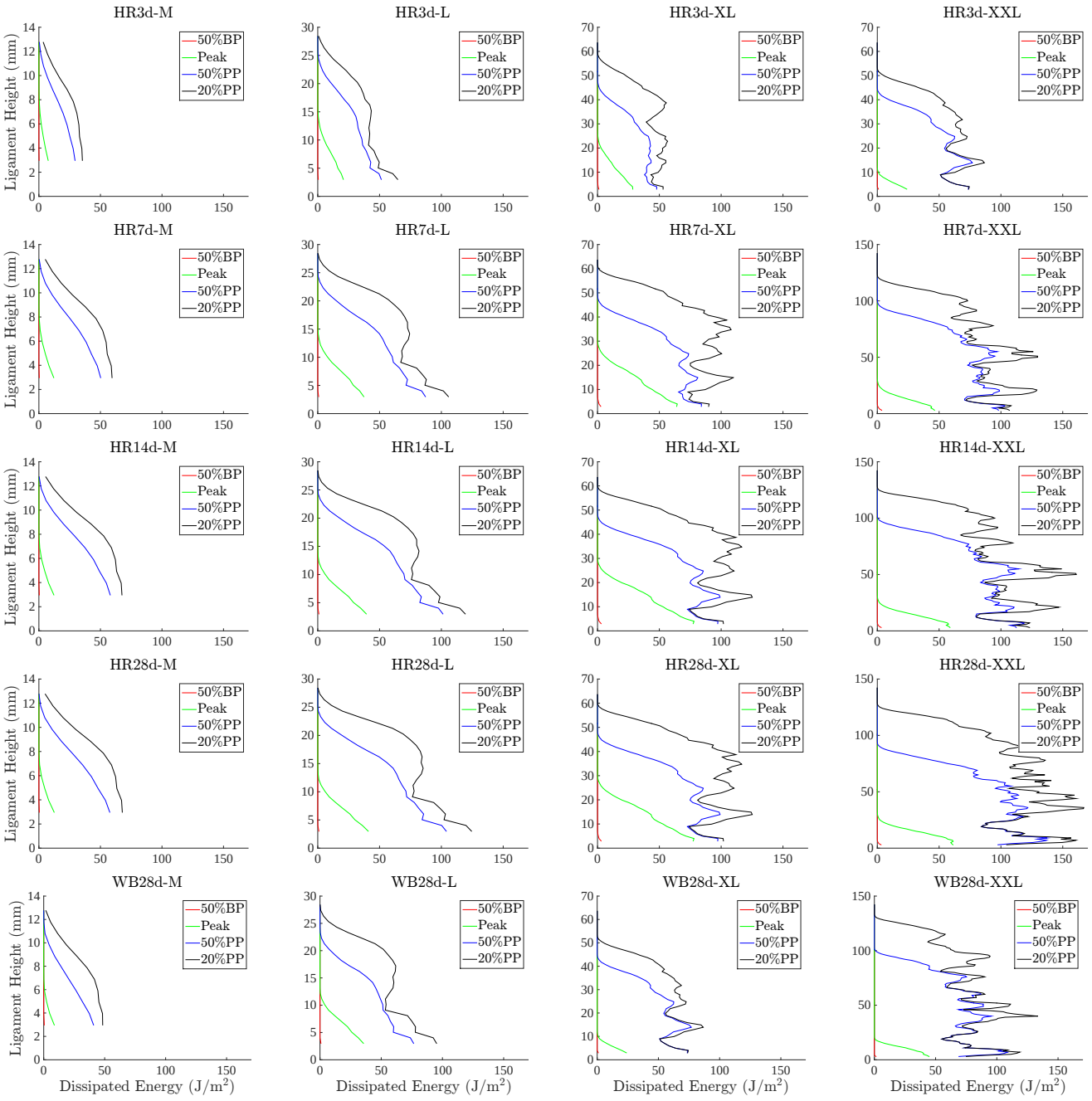

Figure 8: Dissipated energy along ligament from A-LDPM simulations for size effect study; from left to right: size M, L, XL, XXL; top to bottom: age HR3d, HR7d, HR14d, HR28d, WB28d

5 Fracture Characteristics at Early Age

There are a limited number of studies in the literature concerning how fracture energy changes during concrete aging at early ages. Schutter and Taerwe [34] found, for regular concrete with different types of cement under TPB, that the fracture energy increases from 1 day to 28 days of age. Ostergaard [22] also concluded from wedge-splitting-test (WST) on 1 $\sim$ 28 days, utilizing a high performance concrete, that the fracture energy increases while aging. Whereas, Reis [12] conducted TPB tests on PET polymer concrete and concluded that fracture energy decreases from day 1 to day 14. Similarly, Gettu [31] also found that fracture energy decreases from day 4 to 232 days, utilizing a high-strength silica fume concrete with mix proportions close to the UHPC used in this study. Furthermore, Kim et al. [24] observed from wedge-splitting-test an increasing trend of fracture energy for low strength concrete, however, actually increasing then decreasing fracture energy for normal strength and high strength concretes from day 1 to day 28.

Through the available experimental campaign on fracture tests in the literature, a conclusion can be drawn that the fracture energy does not necessarily increase in terms of concrete aging. Furthermore, Wan et al. [1] observed from the TPB fracture tests for the UHPC investigated that the fracture energy first increases then decreases in terms of aging degree. More specifically, the fracture energy initially increases as the cement hydration and silica fume reaction go up and start approaching their asymptotic values under the humidity room curing; This trend reverses as the material further matures and reaches the ultimate properties under hot water bath curing. Note that the theoretical asymptotes of cement hydration and silica fume reaction vary under different curing conditions, which, for 100% humidity room curing, are lower than the values for hot water bath curing. With the aging functions developed by Wan et. al [1] relating mesoscale LDPM parameters and aging degree λ:

$$\text{Normal Modulus: } E_0 = E_0^{\infty} * \lambda \tag{7}$$

$$\text{Tensile Strength: } f_t^{'} = f_t^{'\infty} * \lambda^{n_a} \tag{8}$$

$$\text{Tensile Characteristic Length: } \ell_t = \ell_t^{\infty}(k_a(1-\lambda)+1) \tag{9}$$

The mesoscale fracture energy, $G_t = \ell_t f_t^{'2}/2E_0$, can be derived as a function of aging degree in the following

form:

$$G_t = \lambda^{2n_a} \frac{\ell_t^{\infty} \sigma_t^{\infty 2}}{2E_0^{\infty}} \left(\frac{k_a + 1}{\lambda} - k_a \right) \qquad \propto \quad \lambda^{2n_a} \left(\frac{k_a + 1}{\lambda} - k_a \right) \tag{10}$$

where n_a and k_a are positive constants. Mathematically, G_t can increase or decrease depending on n_a and k_a, which describe the evolution of material properties. This equation, derived from the well structured and experimentally validated HTC-LDPM early age model for UHPC, explains the phenomenon that the fracture energy can have non-monotonous relationship with concrete aging at early age depending on the material. The reason is that the fracture energy is dependent on modulus, tensile characteristic length, and tensile strength, which may evolve at different rates.

The fracture related parameters are plotted in Fig. 9. The tensile characteristic length, ℓ_1, and the tensile strength, f_t', obtained from CSEC and SEL data fitting, as well as mesoscale ℓ_t and σ_t from LDPM simulations are plotted in Fig. 9a&b. The corresponding initial fracture energy, G_f, from CSEC and SEL analysis, as well as the mesoscale fracture energy, G_t, from HTC-LDPM simulations, in terms of aging degree are plotted in Fig. 9c. The corresponding ages and aging degrees are, from left to right, HR3 (0.558), HR7 (0.706), HR14 (0.776), HR28 (0.810), WB14/28 days (0.954). While the initial fracture energy G_f from SEL is close to that of CSEC, the mesoscale G_t calculated as, $G_t = \ell_t \sigma_t^2 / 2E_0$, is about one third of CSEC G_f. The difference is due to different mechanism of energy dissipation. The meso-scale fracture energy G_t is defined as mode I fracture energy under direct tension on single facets, while dissipation in shear is explicitly captured by friction laws. However, G_f, from both CSEC analysis and LDPM local analysis, includes contributions of energy dissipation from both tension and shear inside the fracture process zone, lumped into the cohesive crack. Fig. 9d presents a typical softening curve in a generic stripe of a beam on age WB28d, more specifically, the local stress vs. crack-opening relation for a 4 mm height stripe located at 4-8 mm above the notch tip, and its optimum fit. The local cohesive stress σ_{ch} is obtained from LDPM as the average of the stresses for the facets directly above the notch and within the stripe at each unit time during the simulated test. The local crack opening w is calculated by equation $w(g_d) = \int_0^{g_d} \frac{dg}{\sigma_{ch}(g)}$, where dg_d is the increment of the dissipated energy computed as the work done by the equivalent cohesive stress for an increment of the crack opening, $dg_d = \sigma_{ch}(g_d) dw$ [19]. The optimum fit of such softening curves can be obtained by assuming a cohesive crack law with an initial plateau followed by a smooth curve consisting of the sum of a straight line and an exponential function. The equation of such a curve is $f(w) = f_t'$ for $w \leq w_0$, $f(w) = 0$ for $w \geq w_u$, and $f(w) = f_t'[c_1 - c_2 \frac{w - w_0}{w_{ch}} + (1 - c_1) \exp(-\frac{w - w_0}{w_{ch}})]$ for

w_0<w<w_u [19]. The initial fracture energy describes only the first part of the softening curve (up to a stress drop of 1/3 - 1/2 of the tensile strength) and is defined as the area under its initial tangent. It is calculated as $G_f = \frac{f_t'^2}{2|f'(0)|}$, where $f'(0)$ is the derivative of the softening curve at crack opening equal to zero, or in other words, when $\sigma_{ch} = f_t'$. By plotting and analyzing the softening curves along the ligament for size L, XL, & XXL, the average local initial fracture energy is obtained to be G_f = 44.5 J/m^2 and the local total fracture energy G_F = 93.0 J/m^2 $\cong$ 2.1G_f. Fracture energies along the ligament for size L and XXL on age WB28d are presented as bar plots in Fig. 10a&b respectively. As shown, the local initial fracture energy is roughly constant along the ligament, while the total energy slightly increases then decreases along the ligament, a behavior previously discussed by Cusatis and co-workers [19]. The drop of the total fracture energy is due to the presence of the specimen outer surface that, constraining the propagation of the meso-cracks, induces a reduction of the number of the fractured lattice elements and consequently the width of the fracture process zone. Moreover, the top 20-30% of the ligament endures compressive stresses until late post-peak, thus very low or no energy dissipation is recorded. The local initial fracture energy, G_f, is higher than the LDPM mesoscale fracture energy, $G_t = 21.1$J/m^2, because G_f includes also the energy dissipation due to shear. The total fracture energy, G_F, on the other hand, agrees with the value obtained by work of fracture $G_F \cong 100.6$J/m^2. The relationships of the fracture energies can be concluded as follows: LDPM $G_t \leq$ local $G_f \leq$ SEL $G_f \leq (\cong)\ CSEC\ G_f < G_F$. However, despite the different magnitudes, all fracture energies have the same trend in terms of aging. As shown in Fig. 9 - c, initial fracture energies from HTC-LDPM, CSEC and SEL all increase then decrease in terms of aging degree.

While fracture energy does not have a monotonous relation with concrete aging, the tensile characteristic length, from HTC-LDPM and CSEC & SEL, on the other hand, decreases monotonously with aging degree. Hence, the tensile strength increases monotonously as well with aging [1]. Thus, it is reasonable to conclude that the tensile characteristic length and the tensile strength, instead of fracture energy, are better choices to evaluate the fracture characteristics of concrete, especially under consideration of concrete aging.

Moreover, by evaluating the "magnitude of size effect" along concrete aging, it is found that older concrete tends to have higher "size effect". In Fig. 11, a 3-D contour of nominal stress as a function of aging degree and logarithmic normalized size is presented. The specimen span and height in the size effect study are designed to have scaling factor of $\sqrt{5}$, thus the normalized sizes for M, L, XL, XXL have values of 1, $\sqrt{5}$, 5, and $5\sqrt{5}$

respectively. As shown, the strength difference with respect to size increases as concrete ages. In other words, the size effect increases with concrete aging.

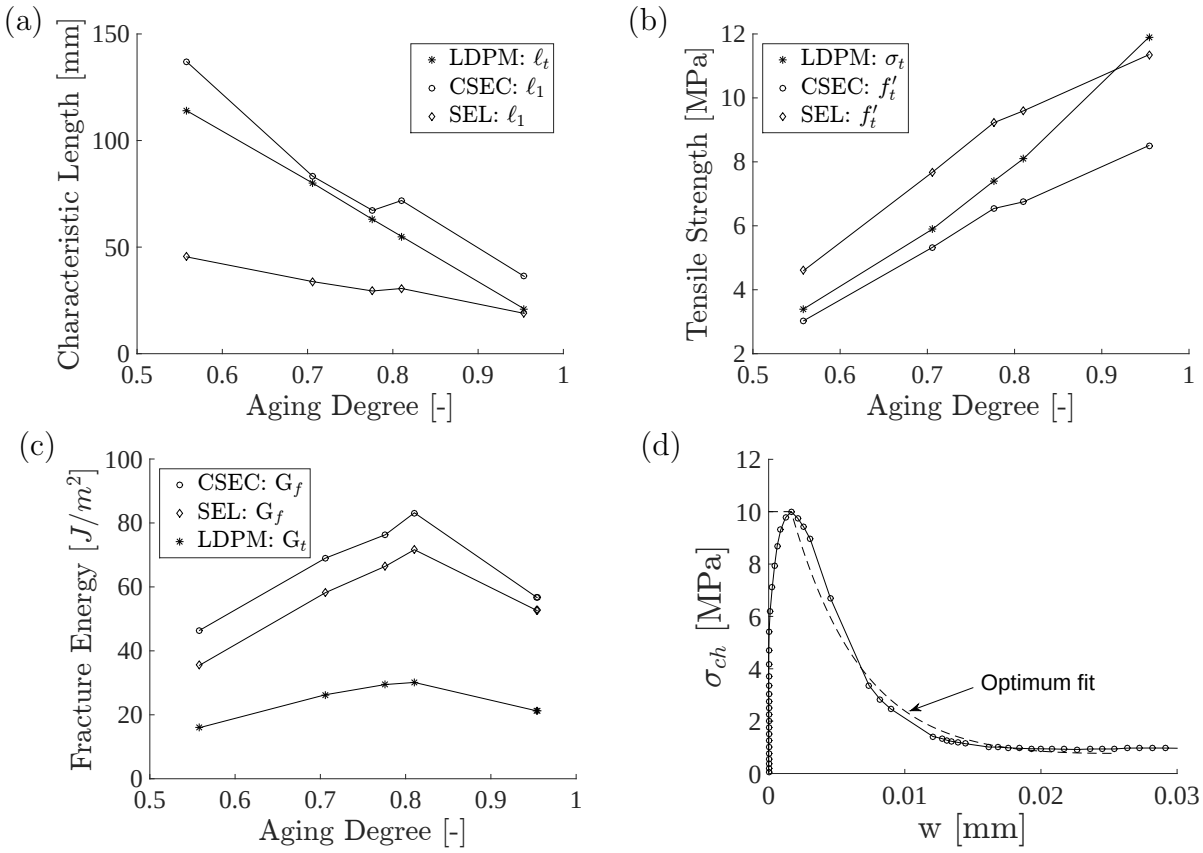

Figure 9: Fracture characteristics at early age: age dependent (a) characteristic length (b) tensile strength (c) fracture energy from A-LDPM simulations and CSEC & SEL analysis; (d) typical softening curve identified in a generic stripe for age WB28d and its optimum fit

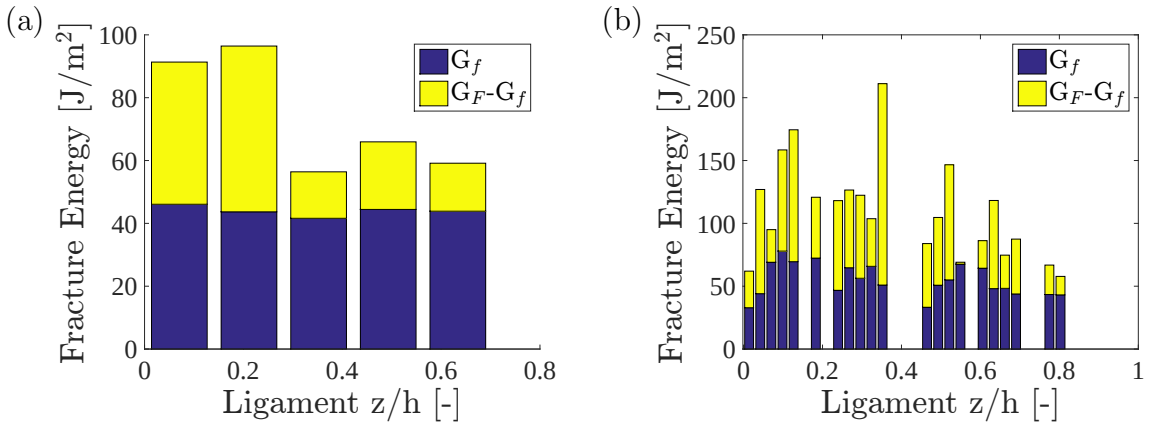

Figure 10: Local fracture energies along the ligament of (a) size L and (b) size XXL

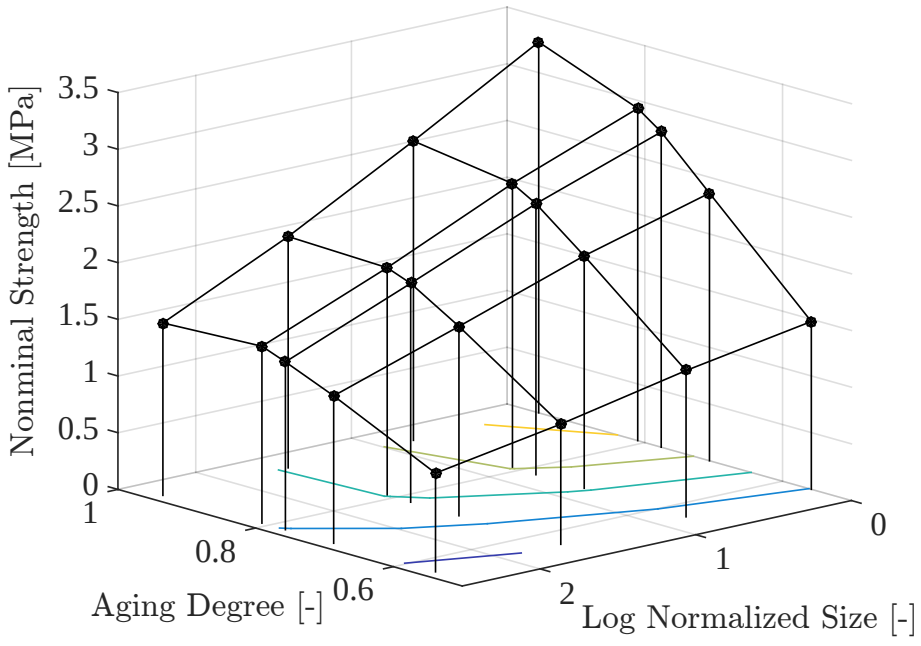

Figure 11: Age dependent size effect

6 Conclusions

In conclusion, the HTC-LDPM framework can accurately capture and predict the age dependent fracture behavior of concrete at early age and its most important consequence, the size effect. The well calibrated and validated model is able to represent the fracture characteristics as evolutions of concrete aging. Furthermore, the *cohesive size effect curve* (CSEC) method is capable of describing the ultimate strength in terms of size for concrete, for both the experiments and the validated predictive simulations.

According to the experimental studies, the numerical simulations as well as the size effect analyses, the following conclusions can be drawn:

- The HTC-LDPM model can accurately capture and predict the age dependent size effect and fracture characteristics for concrete, in this work investigated through three point bending tests.
- Observed from HTC-LDPM, CSEC & SEL analyses, the fracture energy may exhibit a non-monotonous relationship with the maturity of concrete. The reason is that the fracture energy is dependent on modulus, tensile characteristic length, and tensile strength, which may evolve at different rates. Since fracture energy is not an independent material property it is not suitable for the formulation of fracture aging laws.
- The fracture energies by different methods and on different scales are found to have the following relationships: LDPM $G_t \leq$ local $G_f \leq$ SEL $G_f \leq (\cong)\ CSEC\ G_f < G_F$.
- Contrary to fracture energy the tensile characteristic length changes monotonously in all investigated cases and shows a linear decreasing dependence on aging degree for the studied UHPC.
- The CSEC method can fit the size effect data on various early ages with high correlation coefficients above 99%. It can represent the size effect phenomenon of concrete very well and thus can be utilized reliably to predict nominal strength for a broad size and age range outside the laboratory scale.
- In terms of sensitivity of CSEC, obtaining ℓ_1 and G_f is fairly stable against noise in the data; On the other hand, getting f_t' through CSEC can be very sensitive to noise in the data, whereas, exerting upper and lower bounds of the expected range of f_t' can improve its accuracy.

- While the SEL method can fit the size effect data almost as good as CSEC, and their asymptotes coincide with each other for large sizes, SEL solely lacks the representation of plastic limit for small sizes.
- Size effect of concrete is age dependent. The magnitude of size effect increases with concrete aging for the investigated UHPC.

Acknowledgement

The work of the first and last author was supported under National Science Foundation (NSF) Grant CMMI-1237920 to Northwestern University. The work of the first and second author was also supported by the Austrian Federal Ministry of Economy, Family and Youth, and the National Foundation for Research, Technology and Development. The computational component of this research effort was partially sponsored by the US Army Engineer Research Development Center (ERDC) under Grant W912HZ-12-P-0137. Permission to publish was granted by the director of ERDC geotechnical and structural laboratory.

Appendix A - The Mixture Constituents and Curing Procedures

The mixture proportions for the adopted UHPC mix design are reported below in Table 4. The material composition consists of LaFarge Type H cement, F-50 Ottawa sand, Sil-co-sil 75 silica flour, Elkem ES-900W silica fume, ADVA-190 Superplasticizer and tap water. The maximum particle size, 0.6 mm, is limited to that of silica sand, which is a foundry grade Ottawa sand [17]. In the author's previous studies [1], two curing protocols with and without hot water bath curing were explored. A first group of specimens was kept in the humidity room (HR) for 14 days, a second group, instead, was kept in the humidity room for 7 days after which it was placed in hot water bath (WB) at 85°C for another 7 days. After 14 days HR and WB curing, the specimens of both groups were stored at room temperature and average RH of 50% until testing. In this study, the size effect experimental specimens followed the WB curing procedures, while the predictive simulations were ran for both curing routines.

Table 4: Constituents and Mixing Proportions of UHPC CorTuf

Ingredient	Type	Proportion	Weight per kg
Cement	Lafarge Type H	1.0000	0.3497
Sand	F-50	0.9674	0.3383
Silica Flour	Sil-co-sil 75	0.2768	0.0968
Silica Fumes	Elkem ES-900W	0.3890	0.1360
Superplasticizer	ADVA-190	0.0180	0.0063
Water	Tap Water	0.2082	0.0728

Appendix B - The Computational Framework

The proposed hygro-thermo-chemo-mechanical early-age model for cement based concrete consists of two major components: the HTC model and the LDPM with aging material properties.

Hygro-Thermo-Chemical (HTC) model

The behavior of concrete at early age heavily depends on moisture content and temperature. The overall moisture transport can be described through Fick's law that expresses the flux of water mass per unit time $\mathbf{J}$ as a function of the spatial gradient of the relative humidity h. Assuming that evaporable water w_e is a function of relative humidity h, degree of hydration α_c, and degree of silica fume reaction α_s, one can write $w_e = w_e(h, \alpha_c, \alpha_s)$, which represents an age-dependent sorption/desorption isotherm. Consequently, the

moisture mass balance equation reads [15]: $\nabla \cdot (D_h \nabla h) - \frac{\partial w_e}{\partial h}\frac{\partial h}{\partial t} - \left(\frac{\partial w_e}{\partial \alpha_c}\dot{\alpha}_c + \frac{\partial w_e}{\partial \alpha_s}\dot{\alpha}_s + \dot{w}_n\right) = 0$, where D_h is moisture permeability and w_n is nonevaporable water. The enthalpy balance is also influenced by the chemical reactions occurring at the early age. One can write, at least for temperatures not exceeding 100 °C [35], $\nabla \cdot (\lambda \nabla T) - \rho c_t \frac{\partial T}{\partial t} + \dot{\alpha}_s s \tilde{Q}_s^\infty + \dot{\alpha}_c c \tilde{Q}_c^\infty = 0$, where $\tilde{Q}_c^\infty$ = hydration enthalpy, $\tilde{Q}_s^\infty$ = latent heat of silica-fume reaction per unit mass of reacted silica-fume, ρ is the mass density of concrete, λ is the heat conductivity, and c_t is the isobaric heat capacity of concrete.

With the assumption that the thermodynamic force is governed by an Arrhenius-type equation and that the viscosity governing the diffusion of water though the layer of cement hydrates is an exponential function of the hydration extent [36], Cervera et al. [28] proposed the evolution equation for the hydration degree: $\dot{\alpha}_c = A_c(\alpha_c) e^{-E_{ac}/RT}$, and $A_c(\alpha_c) = A_{c1}(\frac{a_{c2}}{\alpha_c^\infty} + \alpha_c)(\alpha_c^\infty - \alpha_c) e^{-\eta_c \alpha_c / \alpha_c^\infty}$, where E_{ac} is the hydration activation energy, R is the universal gas constant, and η_c, A_{c1}, and A_{c2} are material parameters. To account for the situation that the hydration process slows down and may even stop if the relative humidity decreases below a certain value, the equation can be rewritten as: $\dot{\alpha}_c = A_c(\alpha_c)\beta_h(h) e^{-E_{ac}/RT}$, where $\beta_h(h) = [1 + (a - ah)^b]^{-1}$. The function $\beta_h(h)$ is an empirical function proposed by Bažant and Prasannan [39] and a & b are constant model parameters. Similarly, the degree of silica fume (SF) reaction, α_s is introduced [15], $\dot{\alpha}_s = A_s(\alpha_s) e^{-E_{as}/RT}$, and $A_s(\alpha_s) = A_{s1}(\frac{A_{s2}}{\alpha_s^\infty} + \alpha_s)(\alpha_s^\infty - \alpha_s) e^{-\eta_s \alpha_s / \alpha_s^\infty}$, where A_s is the SF normalized affinity, E_{as} is the activation energy of SF reaction, and α_s^∞ is the asymptotic value of the SF reaction degree.

To account for this additional effect from temperature [26], the aging degree λ is typically used and formulated as: $\dot{\lambda} = \left(\frac{T_{max} - T}{T_{max} - T_{ref}}\right)^{n_\lambda} (B_\lambda - 2A_\lambda \alpha)$, where $B_\lambda = [1 + A_\lambda(\alpha_\infty^2 - \alpha_0^2)]/(\alpha_\infty - \alpha_0)$, n_λ and A_λ are model parameters obtained from fitting experimental data, and α is the overall degree of reaction defined as [9]: $\alpha(t) = \frac{\alpha_c(t) c \tilde{Q}_c^\infty + \alpha_s(t) s \tilde{Q}_s^\infty}{c \tilde{Q}_c^\infty + s \tilde{Q}_s^\infty}$.

Age-dependent Lattice Discrete Particle Model

The Lattice Discrete Particle Model (LDPM) is a mesoscale discrete model that simulates the mechanical interaction of coarse aggregate pieces embedded in a cementitious matrix (mortar). In LDPM, rigid body kinematics is used to describe the deformation of the lattice particle system and the displacement jump, $[\![\mathbf{u}_C]\!]$, at the centroid of each facet is used to define measures of strain as $e_N = \frac{\mathbf{n}^{\mathrm{T}}[\![\mathbf{u}_C]\!]}{\ell}$; $e_L = \frac{\mathbf{l}^{\mathrm{T}}[\![\mathbf{u}_C]\!]}{\ell}$; $e_M = \frac{\mathbf{m}^{\mathrm{T}}[\![\mathbf{u}_C]\!]}{\ell}$, where ℓ = interparticle distance; and $\mathbf{n}$, $\mathbf{l}$, and $\mathbf{m}$, are unit vectors defining a local system of reference attached

to each facet.

Next, a vectorial constitutive law governing the behavior of the material is imposed at the centroid of each facet. In the elastic regime, the normal and shear stresses are proportional to the corresponding strains: $t_N = E_N e_N^* = E_N(e_N - e_N^0)$; $t_M = E_T e_M^* = E_T(e_M - e_M^0)$; $t_L = E_T e_L^* = E_T(e_L - e_L^0)$, where $E_N = E_0$, $E_T = \alpha E_0$, $E_0 =$ effective normal modulus, and $\alpha =$ shear-normal coupling parameter; and e_N^0, e_M^0, e_L^0 are mesoscale eigenstrains that might arise from a variety of phenomena such as, but not limited to, thermal expansion, creep, shrinkage, and chemical reactions, e.g. alkali-silica reaction.

For stresses and strains beyond the elastic limit, the LDPM formulation considers the following nonlinear mesoscale phenomena [10]: (1) fracture and cohesion; (2) compaction and pore collapse; and (3) friction.

Fracture and cohesion due to tension and tension-shear. For tensile loading ($e_N^* > 0$), the fracturing behavior is formulated through an effective strain, $e^* = \sqrt{e_N^{*2} + \alpha(e_M^{*2} + e_L^{*2})}$, and stress, $t = \sqrt{t_N^2 + (t_M^2 + t_L^2)/\alpha}$, which define the normal and shear stresses as $t_N = e_N^*(t/e^*)$; $t_M = \alpha e_M^*(t/e^*)$; $t_L = \alpha e_L^*(t/e^*)$. The effective stress t is incrementally elastic ($\dot{t} = E_0\dot{e}$) and must satisfy the inequality $0 \leq t \leq \sigma_{bt}(e,\omega)$ where $\sigma_{bt} = \sigma_0(\omega)\exp\left[-H_0(\omega)\langle e - e_0(\omega)\rangle/\sigma_0(\omega)\right]$, $\langle x\rangle = \max\{x, 0\}$, and $\tan(\omega) = e_N^*/\sqrt{\alpha}e_T^* = t_N\sqrt{\alpha}/t_T$, and $e_T^* = \sqrt{e_M^{*2} + e_L^{*2}}$. The post peak softening modulus is defined as $H_0(\omega) = H_t(2\omega/\pi)^{n_t}$, where H_t is the softening modulus in pure tension ($\omega = \pi/2$) expressed as $H_t = 2E_0/\left(\ell_t/\ell - 1\right)$; $\ell_t = 2E_0G_t/\sigma_t^2$; ℓ is the length of the tetrahedron edge; and G_t is the mesoscale fracture energy. LDPM provides a smooth transition between pure tension and pure shear ($\omega = 0$) with parabolic variation for strength given by $\sigma_0(\omega) = \sigma_t r_{st}^2\Big(-\sin(\omega) + \sqrt{\sin^2(\omega) + 4\alpha\cos^2(\omega)/r_{st}^2}\Big)/[2\alpha\cos^2(\omega)]$, where $r_{st} = \sigma_s/\sigma_t$ is the ratio of shear strength to tensile strength.

Compaction and pore collapse from compression. Normal stresses for compressive loading ($e_N^* < 0$) must satisfy the inequality $-\sigma_{bc}(e_D, e_V) \leq t_N \leq 0$, where σ_{bc} is a strain-dependent boundary depending on the volumetric strain, e_V, and the deviatoric strain, $e_D = e_N - e_V$. The volumetric strain is computed by the volume variation of the Delaunay tetrahedra as $e_V = \Delta V/3V_0$ and is assumed to be the same for all facets belonging to a given tetrahedron. Beyond the elastic limit, $-\sigma_{bc}$ models pore collapse as a linear evolution of stress for increasing volumetric strain with stiffness H_c for $-e_V \leq e_{c1} = \kappa_{c0}e_{c0}$: $\sigma_{bc} = \sigma_{c0} + \langle -e_V - e_{c0}\rangle H_c(r_{DV})$; $H_c(r_{DV}) = H_{c0}/(1 + \kappa_{c2}\langle r_{DV} - \kappa_{c1}\rangle)$; σ_{c0} is the mesoscale compressive yielding stress; $r_{DV} = e_D/e_V$ and κ_{c1}, κ_{c2} are material parameters. Compaction and rehardening occur beyond pore collapse ($-e_V \geq e_{c1}$). In this

case one has $\sigma_{bc} = \sigma_{c1}(r_{DV})\ \exp\left[(-e_V - e_{c1})H_c(r_{DV})/\sigma_{c1}(r_{DV})\right]$ and $\sigma_{c1}(r_{DV}) = \sigma_{c0} + (e_{c1} - e_{c0})H_c(r_{DV})$.

Friction due to compression-shear. The incremental shear stresses are computed as $\dot{t}_M = E_T(\dot{e}^*_M - \dot{e}^{*p}_M)$ and $\dot{t}_L = E_T(\dot{e}^*_L - \dot{e}^{*p}_L)$, where $\dot{e}^{*p}_M = \dot{\xi}\partial\varphi/\partial t_M$, $\dot{e}^{*p}_L = \dot{\xi}\partial\varphi/\partial t_L$, and ξ is the plastic multiplier with loading-unloading conditions $\varphi\dot{\xi} \leq 0$ and $\dot{\xi} \geq 0$. The plastic potential is defined as $\varphi = \sqrt{t_M^2 + t_L^2} - \sigma_{bs}(t_N)$, where the nonlinear frictional law for the shear strength is assumed to be $\sigma_{bs} = \sigma_s + (\mu_0 - \mu_\infty)\sigma_{N0}[1 - \exp(t_N/\sigma_{N0})] - \mu_\infty t_N$; σ_{N0} is the transitional normal stress; μ_0 and μ_∞ are the initial and final internal friction coefficients.

Besides the compatibility and constitutive equations discussed above, the governing equations of the LDPM framework are completed through the equilibrium equations of each individual particle.

The proposed aging functions relating the mesoscale material parameters read $E_0 = E_0^\infty\lambda$; $\sigma_t = \sigma_t^\infty\lambda^{n_a}$; $\sigma_c = \sigma_c^\infty\lambda^{n_a}$; $\sigma_{N0} = \sigma_N^\infty\lambda^{n_a}$; $\ell_t = \ell_t^\infty(k_a(1-\lambda)+1)$, where n_a and k_a are positive constants. As seen, the normal modulus, E_0, which is related to the elastic modulus, is assumed to have a linear relation with aging degree λ. Tensile strength, σ_t, compressive yielding stress, σ_c, and transitional stress, σ_{N0}, on the other hand, are assumed to have power-law type relations with aging degree. Lastly, the tensile characteristic length, ℓ_t, is assumed to be a linear decreasing function with aging degree, to simulate the well known brittleness increase with age. All the aging functions are formulated such that the corresponding parameters approach their asymptotic values for λ approaching the value of 1. The other LDPM mesoscale parameters, are assumed age-independent due to a lack of relevant experimental data on the response in compression under confinement.

References

[1] L. Wan, R. Wendner, B. Liang, G. Cusatis. Analysis of the Behavior of Ultra-High-Performance-Concrete at Early Age, Cement and Concrete Composites, 2016. doi: 10.1016/j.cemconcomp.2016.08.005

[2] L. Wan, R. Wendner, and G. Cusatis. Behavior of Ultra-High-Performance Concrete at Early age: Experiments and Simulations. First International Interactive Symposium on UHPC, 2016. doi: 10.21838/uhpc.2016.7

[3] L. Wan, R. Wendner, and G. Cusatis. A Novel Material for In Situ Construction on Mars: Experiments and Numerical Simulations. Construction and Building Materials, 120 (2016) 222-231. doi:10.1016/j.conbuildmat.2016.05.046

[4] L. Wan, R. Wendner, G. Cusatis, A Hygro-Thermo-Chemo Mechanical Model for the Simulation of Early Age Behavior of Ultra-High-Performance Concrete, CONCREEP 10: pp. 166-175, Vienna, Austria, Sep 2015, doi: 10.1061/9780784479346.020

[5] G. Boumakis, M. Marcon, L. Wan, R. Wendner, Creep and Shrinkage in Fastening Systems, CONCREEP 10: pp. 657-666, 2015, doi: 10.1061/9780784479346.079.

[6] J. Smith, G. Cusatis, D. Pelessone, E. Landis, J. O'Daniel, J. Baylot. Discrete modelling of ultra-high-performance concrete with application to projectile penetration International Journal of Impact Engineering 65, 2014, 13-32.

[7] L. Jendele, V. Smilauer, and J. Cervenka. Multiscale hydro-thermo-mechanical model for early-age and mature concrete structures. Advances in Engieering Software 72 (2014) 134-146.

[8] G. Sciume, F. Benboudjema, C. De Sa, F. Pesavento, Y. Berthaud, B.A. Schrefler. A multiphysics model for concrete at early age applied to repairs problems. Engineering Structures 57 (2013) 374-387.

[9] G. Di Luzio and G. Cusatis. Solidification-microprestress-microplane (SMM) theory for concrete at early age: Theory, validation and application. International Journal of Solids and Structures 50, 957-975, 2013.

[10] G. Cusatis, D. Pelessone, and A. Mencarelli. Lattice discrete particle model (LDPM) for failure behavior of concrete. I: Theory. Cement Concrete Composites, 33(9), 881-890, (2011).

[11] G. Cusatis, D. Pelessone, and A. Mencarelli. Lattice discrete particle model (LDPM) for failure behavior of concrete. II: Calibration and validation. Cement Concrete Composites, 33(9), 891-905, (2011).

[12] J.M.L Reis. Effect of aging on the fracture mechanics of unsaturated polyester based on recycled PET polymer concrete. Material Science and Engineering A. 528 (2011) 3007-3009.

[13] G. Cusatis, E. A. Schauffert. Cohesive crack analysis of size effect. Engineering Facture Mechanics 76 (2009) 2163-2173.

[14] Z. P. Bažant, Q. Yu. Universal size effect law and effect of crack depth on quasi-brittle structure strength Journal of Engineering Mechanics, ASCE, Feb, 2009.

[15] G. Di Luzio and G. Cusatis. Hygro-thermo-chemical modeling of high performance concrete. I: Theory. Cement and Concrete composites 31 (5), 301-308, 2009.

[16] G. Di Luzio and G. Cusatis. Hygro-thermo-chemical modeling of high performance concrete. II: Numerical implementation, calibration, and validation. Cement and Concrete composites 31 (5), 309-324, 2009.

[17] M. J. Roth, T. S.Rushing, O. G. Flores, D. K. Sham, and J. W. Stevens. Laboratory Characterization of Cor-Tuf Flexural and Splitting Tensile Properties U.S. Army Engineer Research and Development Center, Vicksburg, MS. 2009.

[18] L. Cedolin, G. Cusatis Identification of concrete fracture parameters through size effect experiments. Cem Concr Comp 2008; 30(9):788-797.

[19] G. Cusatis, L. Cedolin Two-scale study of concrete fracturing behavior. Eng. Frac. Mech. 74 (2007) 3-17.

[20] D. Gawin, F. Pesavento and B.A. Schrefler. Hygro-thermo-chemo-mechanical modelling of concrete at early ages and beyond, Part I: hydration and hygrothermal phenomena. Int J Numer Methods Eng 2006;67:299-331.

[21] D. Gawin, F. Pesavento and B.A. Schrefler. Hygro-thermo-chemo-mechanical modelling of concrete at early ages and beyond, Part II: shrinkage and creep of concrete. Int J Numer Methods Eng 2006;67:332-363.

[22] L. Ostergaard, D. Lange, H. Stang. Early-age stress-crack opening relationships for high performance concrete. Cement & Concrete Composites 26 (2004) 563-572.

[23] R. Lackner and H. A. Mang. Chemoplastic material model for the simulation of early-age cracking: From the constitutive law to numerical analyses of massive concrete structures. Cement Concrete Composites 2004, 26: 551-562.

[24] J-K. Kim, Y. Lee, S-T Yi. Fracture characteristics of concrete at early ages. Cement and Concrete Research 34(2004) 507-519.

[25] O. Bernard, F-J. Ulm, and E. Lemarchand. A multi scale micromechanics-hydration model for the early-age elastic properties of cement-based materials. Cement and Concrete Research, 33, 1293-1309, 2003.

[26] M. Cervera, J. Oliver, and T. Prato. Simulation of construction of RCC dams. I: temperature and aging. Journal of Structural Engineering. Vol. 126, No. 9, September 2000.

[27] M. Cervera, J. Oliver, and T. Prato. Simulation of construction of RCC dams. II: stress and damage. Journal of Structural Engineering. Vol. 126, No. 9, September 2000.

[28] M. Cervera, J. Oliver, and T. Prato. Thermo-chemo-mechanical model for concrete. I: hydration and aging. Journal of Engineering Mechanics, September 1999.

[29] M. Cervera, J. Oliver, and T. Prato. Thermo-chemo-mechanical model for concrete. II: damage and creep. Journal of Engineering Mechanics, September 1999.

[30] Z.P. Bažant, J. Planas. Fracture and size effect in concrete and other quasibrittle materials. Boca Raton, Florida 33431; CRC Press LLC; 1998.

[31] R. Gettu, V.O. Garcia-Alvarez, A. Aguado. Effect of aging on the fracture characteristics and brittleness of a high-strength concrete. Cement and Concrete Research, Vol. 28. No. 3. pp. 349-355, 1998.

[32] F-J. Ulm and O. Coussy. Couplings in early-age concrete: from material modeling to structural design International Journal of Solids and Structures, Volume 35, Number 31, 4295-4311 (17), 1998.

[33] J. Planas, G.V. Guinea, M. Elices. Generalized size effect equation for quasibrittle materials. Fatigure Fract Engng Mater Struct 1997; 20(5): 671-687.

[34] G. D. Schutter, L. Taerwe. Fracture energy of concrete at early ages. Materials and Structures, RELIM, March 1997, 67-71.

[35] Z. P. Bažant and M. F. Kaplan. Concrete at high temperatures: material properties and mathematical models. London: Longman Addison-Wesley; 1996.

[36] F-J. Ulm, and O. Coussy. Modeling of thermo-chemical-mechanical couplings of concrete at early age. Journal of Engineering Mechanics, ASCE 1995; 121(7): 785-794. 1995.

[37] J.Y. Pastor, G. Guinea, J. Planas, M. Elices. Nueva expresin del factor de intensidad de tensiones para la probeta de flexin en tres puntos. Anales de Mecnica de la Fractura, 12, 85∼90. 1995.

[38] J. Planas, M. Elices. Asymptotic analysis of a cohesive crack 1. Theoretical background. International Journal of Fracture. 1992; 55: 153-177.

[39] Z. P. Bažant, and S. Prasannan. Solidification theory for concrete creep. I: formulation. Journal of Engineering Mechanics, ASCE 115, 1691-1703. 1989.

[40] J. Planas, M. Elices. Towards a measure of G_F : an analysis of experimental results. Wittman FH, editor. Fracture toughness and fracture energy of concrete. Amsterdam: Elsevier; 1986.

[41] Z. P. Bažant. Size effect in blunt fracture: concrete, rock, metal. ASCE Journal of Engineering Mechanics 1984; 110: 518-535.

[42] J. Byfors. Plain concrete at early ages. Res. Rep. F3:80. Swedish Cement and Concrete Res. Inst., Stockholm, Sweden, 1980.

[43] M. Regourd and E. Gauthier. "Comportement des eiments soumis au durcissement accelere [Behaviour of cement under accelerated hardening]. Annales de l'ITBTP. Paris. France, 31'7, 65-96, 1980.